

# Studies of granularity of a hadronic calorimeter for tens-of-TeV jets at a 100 TeV $pp$ collider

C.-H. Yeh<sup>a</sup>, S.V. Chekanov<sup>b</sup>, A.V. Kotwal<sup>c,d</sup>, J. Proudfoot<sup>b</sup>, S. Sen<sup>c</sup>, N.V. Tran<sup>d</sup>,  
S.-S. Yu<sup>a</sup>

<sup>a</sup> *Department of Physics, National Central University, Chung-Li, Taoyuan City 32001, Taiwan*

<sup>b</sup> *HEP Division, Argonne National Laboratory, 9700 S. Cass Avenue, Argonne, IL 60439, USA.*

<sup>c</sup> *Department of Physics, Duke University, USA*

<sup>d</sup> *Fermi National Accelerator Laboratory*

<sup>e</sup> *Department of Physics, Michigan State University, 220 Trowbridge Road, East Lansing, MI 48824*

---

## Abstract

Jet substructure of hadronic jets with transverse momenta in the range from 2.5 TeV to 20 TeV were studied using several designs for spacial size of calorimeter cells. The studies using full simulation of calorimeter response complimented with the reconstruction of calorimeter clusters for jet reconstruction. The results unambiguously indicate that performance of jet substructure reconstruction improves with reducing the cell sizes.

*Keywords:* multi-TeV physics,  $pp$  collider, future hadron colliders, FCC, SppC

---

## 1. Introduction

Particle collisions at energies beyond those attained at the LHC will lead to many challenges for detector technologies. Future experiments, such as high-energy LHC (HE-LHC), future circular  $pp$  colliders of the European initiative, FCC-hh [1] and the Chinese initiative, SppC [2] will be required to measure high-momentum bosons ( $W$ ,  $Z$ ,  $H$ ) and top quarks with strongly collimated decay products that form jets. Studies of jet substructure can help identify such particles.

The reconstruction of jet substructure variables for collimated jets with transverse momentum above 10 TeV require an appropriate detector design. The most important for reconstruction of such jets are tracking and calorimeter. Recently, a number of studies [3, 4, 5] have been discussed using various fast simulation tools, such as Delphes [6], in which momenta of particles are smeared to mimic detector response.

A major step towards the usage of full Geant4 simulation to verify the granularity requirements for calorimeters was made in [7]. The studies included in this paper have illustrated a significant impact of granularity of electromagnetic (ECAL) and hadronic (HCAL) calorimeters on the shape of hadronic showers calculated using calorimeter

---

*Email addresses:* jwzuzelski18@gmail.com (C.-H. Yeh), chekanov@anl.gov (S.V. Chekanov), ashutosh.kotwal@duke.edu (A.V. Kotwal), proudfoot@anl.gov (J. Proudfoot), sourav.sen@duke.edu (S. Sen), ntran@fnal.gov (N.V. Tran), syu@cern.ch (S.-S. Yu)

hits for two particles separated by some angle. It was concluded that high granularity is essential in resolving two close-by particles for energies above 100 GeV.

This paper makes another step in understanding of this problem in terms of high-level physics quantities typically used in physics analyses. Similar to the studies presented in [7], this paper is based on a full Geant4 simulation with realistic jet reconstruction.

## 2. Simulation of detector response and event reconstruction

The description of the detector and software used for this paper is discussed in [7]. We use the SiFCC detector geometry with a software package that represents a versatile environment for simulations of detector performance, testing new technology options, event reconstruction techniques for future 100 TeV colliders.

The GEANT4 (version 10.3) [8] simulation of calorimeter response was complemented with the full reconstruction of calorimeter clusters formed by the Pandora algorithm [9, 10]. Calorimeter clusters were built from calorimeter hits in the ECAL and HCAL after applying the corresponding sampling fractions. No other corrections are applied. Hadronic jets were reconstructed with the FASTJET package [11] using the anti- $k_T$  algorithm [12] with a distance parameter of 0.5.

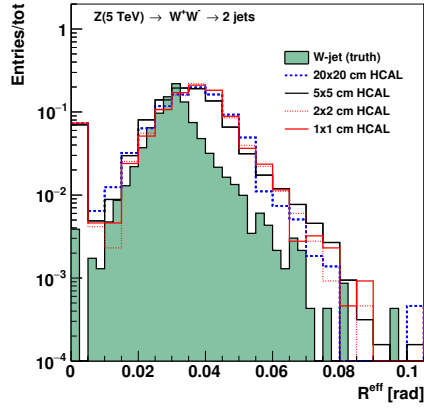
In the following discussion, we use the simulations of a heavy  $Z'$  boson, a hypothetical gauge boson that arises from extensions of the electroweak symmetry of the Standard Model. The  $Z'$  bosons were simulated with the masses,  $M = 5, 10, 20$  and 40 TeV. The lowest value represents a typical mass that is within the reach of the LHC experiments. The value 40 TeV represents the physics reach for a 100 TeV collider. The  $Z'$  particles are forced to decay to two light-flavor jets ( $q\bar{q}$ ),  $W^+W^-$  or  $t\bar{t}$ , where  $W$  and  $t$  decay hadronically. In all such scenarios, two highly boosted jets are produced, which are typically back-to-back in the laboratory frame. Typical transverse momenta of such jets are  $\simeq M/2$ . The main difference between considered decay types lays in different jet substructure. In the case of the  $q\bar{q}$  decays, jets do not have any internal structure. In the case of  $W^+W^-$ , each jet originates from  $W$ , thus it has two subjects because of the decay  $W \rightarrow q\bar{q}$ . In the case of hadronic top decays, jets have three subjects due to the decay  $t \rightarrow W^+b \rightarrow q\bar{q}b$ . The signal events were generated using the PYTHIA8generator with the default settings, ignoring interference with SM processes. The event samples used in this paper are available from the HepSim database [13].

## 3. Studies of jet properties

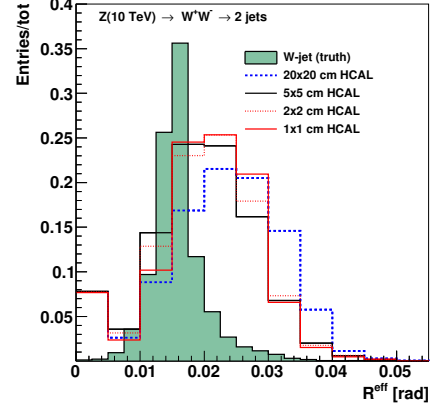
First let us consider several variables that represent jet substructure using different types of calorimeter granularity. The question we want to answer is how close the reconstructed jet substructure variables to the input "truth" value that are reconstructed using input particles directly from the PYTHIA8generator.

The effective radius is the average of the energy weighted radial distance in  $\eta - \phi$  space of jet constituents. Recently, it has been studied for multi-TeV jets in Ref.[14].

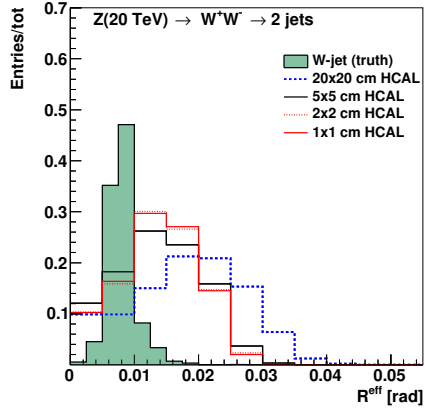
Let us study the effect of granularity on jet splitting scales. A jet  $k_T$  splitting scale [15] is defined as a distance measure used to form jets by the  $k_T$  recombination algorithm [16, 17]. This has been studied by ATLAS [18], and more recently in the context of 100



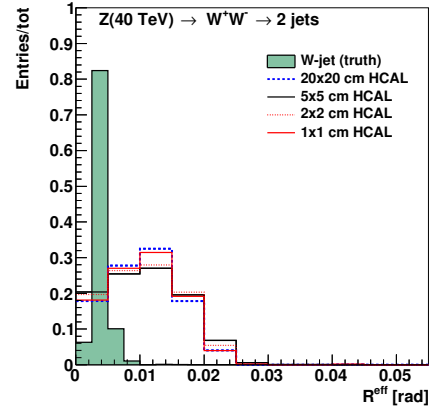
(a) 5 TeV



(b) 10 TeV



(c) 20 TeV



(d) 40 TeV

Figure 1: Jet effective radius for different jet transverse momenta and HCAL granularities.

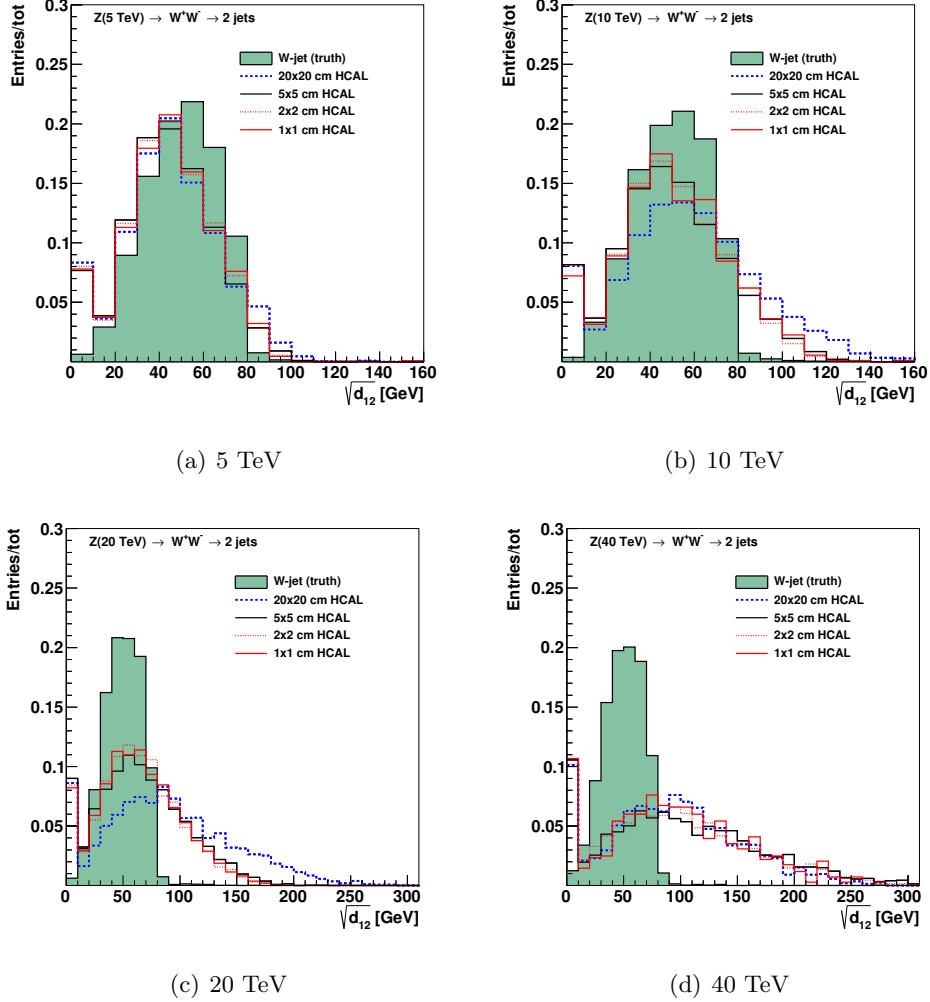


Figure 2: Jet splitting scale for different jet transverse momenta and HCAL granularity.

TeV physics [14]. The distribution of the splitting scale  $\sqrt{d_{12}} = \min(p_T^1, p_T^2) \times \delta R_{12}$  [18] at the final stage of the  $k_T$  clustering, where two subjets are merged into the final one, is shown in Fig. 2.

### 3.1. Jet subjettiness

We recall that  $N$ -subjettiness [19],  $\tau_N$ , of jets has been proposed as a class of variables with which to study the decay products of a heavy particle inside jets.  $\tau_N$  is a measure of the degree to which a jet can be considered as being composed of  $N$   $k_T$ -subjets [19]. The variable  $\tau_{32}$ , defined as the ratio of the  $N$ -subjettiness variables  $\tau_3/\tau_2$ , is particularly sensitive to hadronically-decaying top-quark initiated jets. The variable,  $\tau_{21} \equiv \tau_2/\tau_1$  can be used to reject background from  $W/Z$  decays. These variables do not strongly correlate with jet mass and can provide an independent check for the presence of top quarks. The jet substructure variables were obtained by re-running the

71  $k_T$  algorithm over the jet constituents of anti- $k_T$  jets.

## 72 4. Study of detector performance with soft drop mass

73 In this section, we use the jet mass computed with a specific algorithm, soft drop  
74 declustering, to study the performance of detector with various detector cell sizes and  
75 center-of-mass (c.m.) energies.

### 76 4.1. The technique of soft drop declustering

77 The soft drop declustering [20] is a grooming method that removes soft wide-  
78 angle radiation from a jet. The constituents of a jet  $j_0$  are first reclustered using  
79 the Cambridge-Aachen (C/A) algorithm [21, 22]. Then, the jet  $j_0$  is broken into two  
80 subjets  $j_1$  and  $j_2$  by undoing the last stage of C/A clustering. If the subjets pass  
81 the following soft drop condition, jet  $j_0$  is the final soft-drop jet. Otherwise, the algo-  
82 rithm redefines  $j_0$  to be the subjet with larger  $p_T$  (among  $j_1$  and  $j_2$ ) and iterates the  
83 procedure.

$$\frac{\min(p_{T1}, p_{T2})}{p_{T1} + p_{T2}} > z_{\text{cut}} \left( \frac{\Delta R_{12}}{R_0} \right)^\beta, \quad (1)$$

84 where  $p_{T1}$  and  $p_{T2}$  are the transverse momenta of the two subjets,  $z_{\text{cut}}$  is soft drop  
85 threshold,  $\Delta R_{12}$  is the distance between the two subjets in the rapidity-azimuth angle  
86 plane ( $y$ - $\phi$ ),  $R_0$  is the characteristic radius of the original jet, and  $\beta$  is the angular  
87 exponent.

88 In our study, we compare the performance of future detector when setting  $\beta = 0$   
89 versus when setting  $\beta = 2$ . For  $\beta = 0$ , the soft drop condition depends only on the  $z_{\text{cut}}$ .  
90 For  $\beta = 2$ , the condition depends on the angular distance between the two subjets and  
91  $z_{\text{cut}}$  and the algorithm becomes infrared and collinear safe.

### 92 4.2. Analysis method

93 We employ the following method to quantify the detector performance and find out  
94 the cell size that gives the best separation power to distinguish signal from background.  
95 For each configuration of detector and c.m. energy, we draw the receiver operating  
96 characteristic (ROC) curves in which the x-axis is the signal efficiency ( $\epsilon_{\text{sig}}$ ) and y-axis  
97 is the inverse of background efficiency ( $1/\epsilon_{\text{bkg}}$ ). In order to scan the efficiencies of soft  
98 drop mass cuts, we vary the mass window as follows. We first look for the median  
99 bin  $i_{\text{med}}$ <sup>1</sup> of the soft drop mass histogram from simulated signal events. Taking the  
100 right boundary of bin  $i_{\text{med}}$  as the center of mass window  $x_{\text{center}}$ , we start increasing the  
101 width of mass window symmetrically on the left and on the right of  $x_{\text{center}}$ , in steps of  
102 5 GeV, i.e. the narrowest mass window is  $[x_{\text{center}} - 5, x_{\text{center}} + 5]$ . If one side reaches  
103 the boundary of the mass histogram, we only increase the width on the other side, also  
104 in steps of 5 GeV. For each mass window, there will be corresponding  $\epsilon_{\text{sig}}$  and  $\epsilon_{\text{bkg}}$ ,  
105 which gives a point in the ROC curves.

<sup>1</sup>The integral from bin 0 to bin  $i_{\text{med}}$  ( $i_{\text{med}} - 1$ ) should be greater (less) than half of the total number of events. Note, the bin width is 5 GeV.

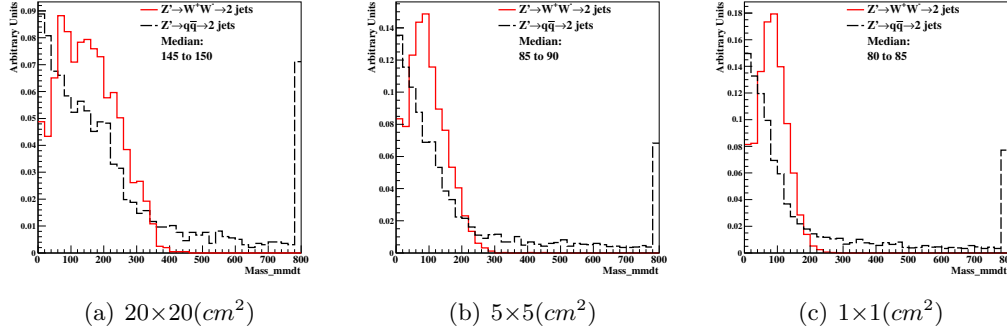


Figure 3: Distributions of soft drop mass for  $\beta=0$ , with 20 TeV c.m. energies and three different detector cell sizes:  $20 \times 20$ ,  $5 \times 5$ , and  $1 \times 1$  ( $cm^2$ ). The signal (background) process is  $Z' \rightarrow WW$  ( $Z' \rightarrow q\bar{q}$ ).

#### 4.3. Results and conclusion

Figures 3, 5, 7, and 9 present the distributions of soft drop mass for  $\beta = 0$  and  $\beta = 2$  with different c.m. energies and detector cell sizes; the signals considered are  $Z' \rightarrow WW$  and  $Z' \rightarrow t\bar{t}$ . In Figs. 4, 6, 8, and 10, ROC curves from different detector cell sizes are compared for each c.m. energy, respectively.

Figures 4 and 6 show that for  $\beta = 0$  the smallest detector cell size,  $1 \text{ cm} \times 1 \text{ cm}$ , has the best separation power at  $\sqrt{s} = 5, 10$ , and 20 TeV when the signal is  $Z' \rightarrow WW$  and at  $\sqrt{s} = 10$  and 20 TeV when the signal is  $Z' \rightarrow t\bar{t}$ . On the contrary, Figs. 8 and 10 show that for  $\beta = 2$  the smallest detector cell size does not have improvements in the separation power with respect to those with larger cell sizes. In fact, the performances of the three cell sizes are similar. In addition, sometimes bigger detector cell sizes,  $5 \text{ cm} \times 5 \text{ cm}$  or  $20 \text{ cm} \times 20 \text{ cm}$  have the best separation power.

We also find compared to  $\beta = 2$ , soft drop mass with  $\beta = 0$  has better performance for distinguishing signal from background. Therefore, we will apply requirements on this variable when studying the other jet substructure variables.

## 5. Study of detector performance with jet substructure variables

In this section, we use several jet substructure variables to study the performance of detector with various detector cell sizes and c.m. energies.

### 5.1. $N$ -subjettiness

The variable  $N$ -subjettiness [19], denoted by  $\tau_N$ , is designed to “count” the number of subjet(s) in a large radius jet so to separate signal jets from decays of heavy bosons and background jets from QCD processes. The  $\tau_N$  is the  $p_T$ -weighted angular distance between each jet constituent and the closest subjet axis:

$$\tau_N = \frac{1}{d_0} \sum_k p_{T,k} \min\{\Delta R_{1,k}, \Delta R_{2,k}, \dots, \Delta R_{N,k}\}, \quad (2)$$

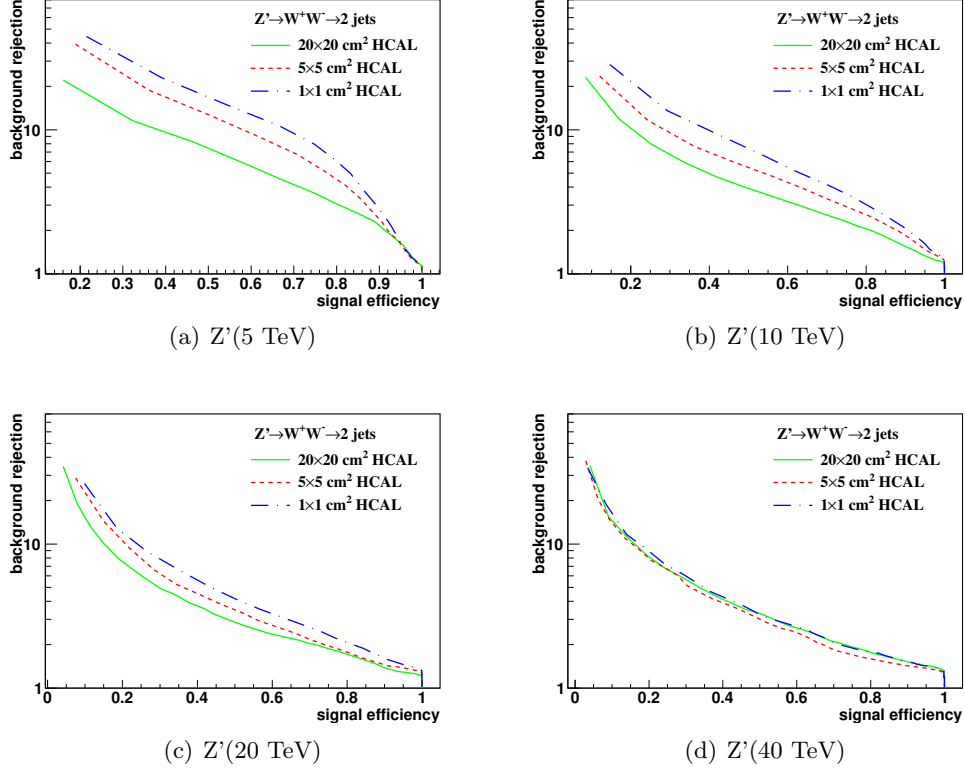


Figure 4: The ROC curves of soft drop mass selection for  $\beta=0$  with 5, 10, 20, 40 TeV c.m. energies. Three different detector cell sizes are compared:  $20 \times 20$ ,  $5 \times 5$ , and  $1 \times 1$  ( $\text{cm}^2$ ). The signal (background) process is  $Z' \rightarrow WW$  ( $Z' \rightarrow q\bar{q}$ ).

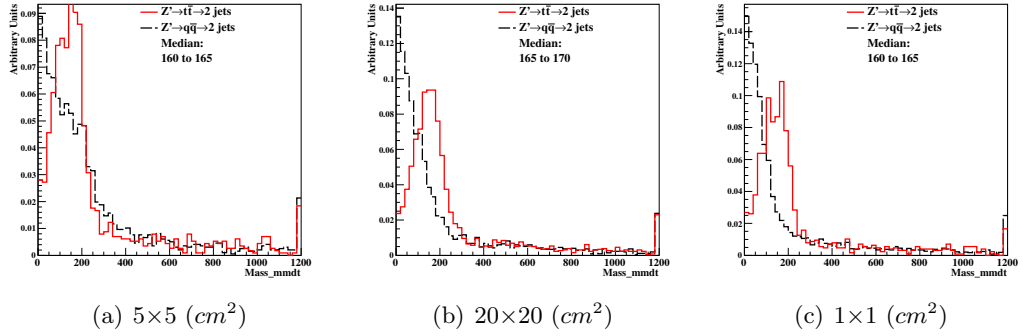


Figure 5: Distributions of soft drop mass for  $\beta=0$ , with 20 TeV c.m. energies and three different detector cell sizes:  $20 \times 20$ ,  $5 \times 5$ , and  $1 \times 1$  ( $\text{cm}^2$ ). The signal (background) process is  $Z' \rightarrow t\bar{t}$  ( $Z' \rightarrow q\bar{q}$ ).

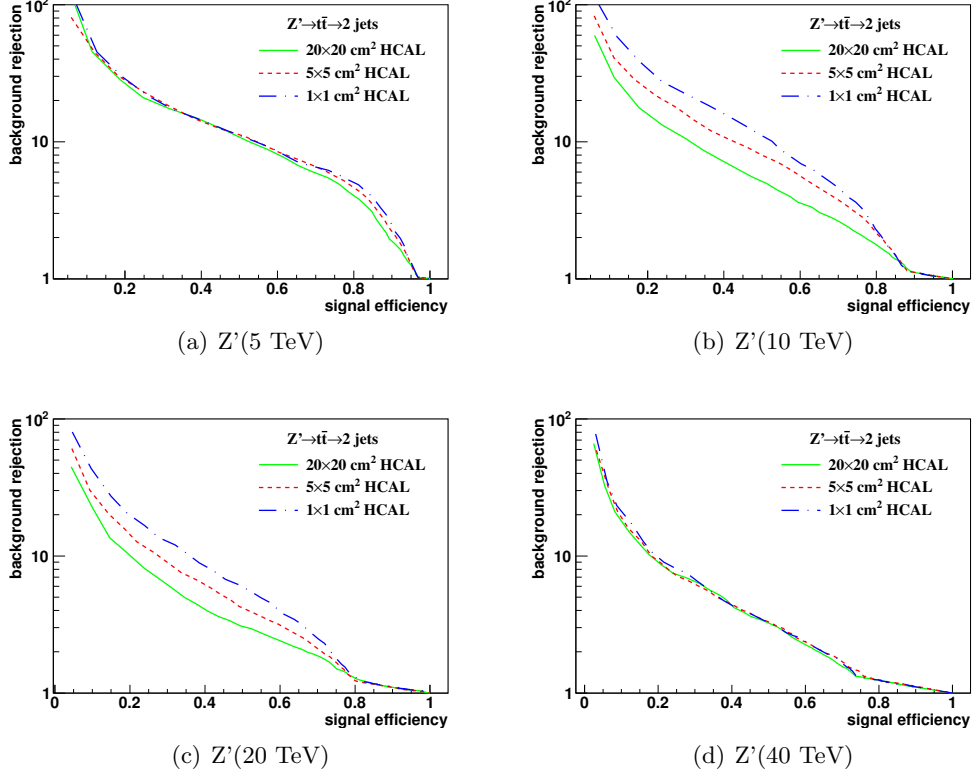


Figure 6: The ROC curves of soft drop mass selection for  $\beta=0$  with 5,10, 20, 40 TeV c.m. energies. Three different detector cell sizes are compared:  $20 \times 20$ ,  $5 \times 5$ , and  $1 \times 1$  ( $\text{cm}^2$ ). The signal (background) process is  $Z' \rightarrow t\bar{t}$  ( $Z' \rightarrow q\bar{q}$ ).

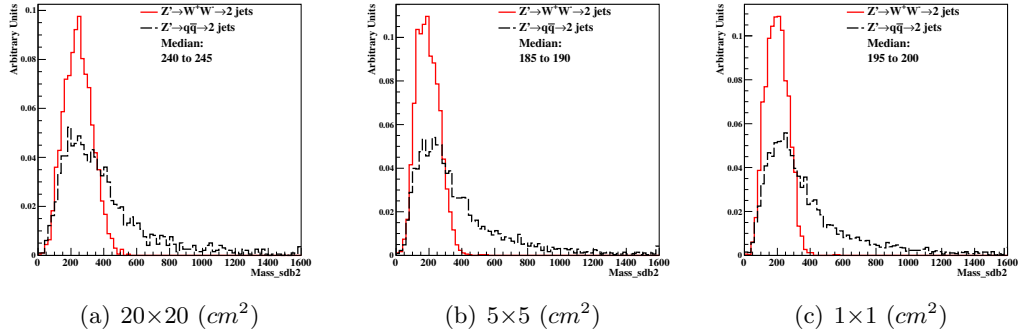


Figure 7: Distributions of soft drop mass for  $\beta=2$ , with 20 TeV c.m. energies and three different detector cell sizes:  $20 \times 20$ ,  $5 \times 5$ , and  $1 \times 1$  ( $\text{cm}^2$ ). The signal (background) process is  $Z' \rightarrow WW$  ( $Z' \rightarrow q\bar{q}$ ).



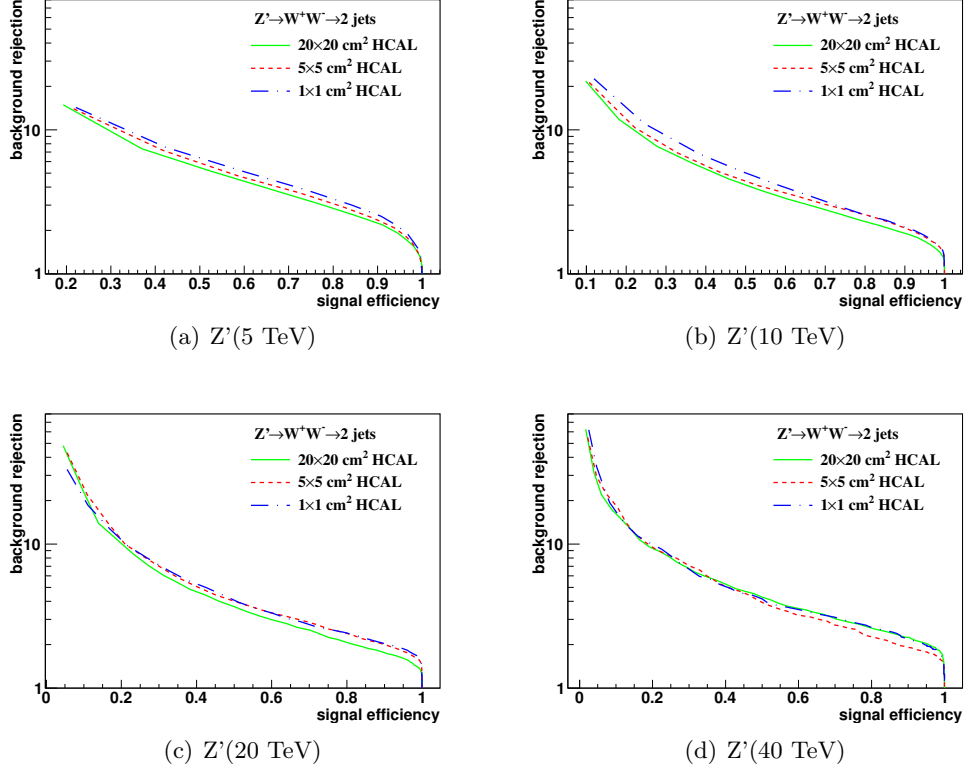


Figure 8: The ROC curves of soft drop mass selection for  $\beta=2$  with 5, 10, 20, 40 TeV c.m. energies. Three different detector cell sizes are compared:  $20 \times 20$ ,  $5 \times 5$ , and  $1 \times 1$  ( $\text{cm}^2$ ). The signal (background) process is  $Z' \rightarrow WW$  ( $Z' \rightarrow q\bar{q}$ ).

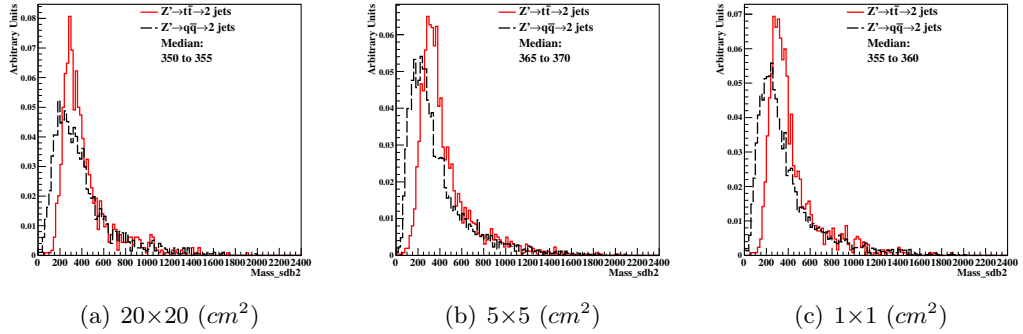
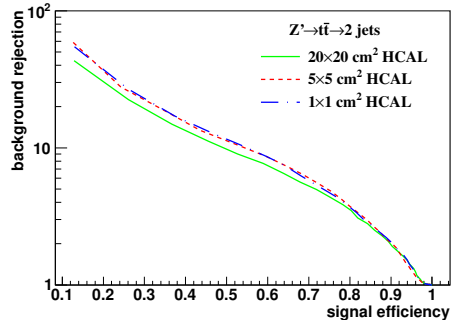
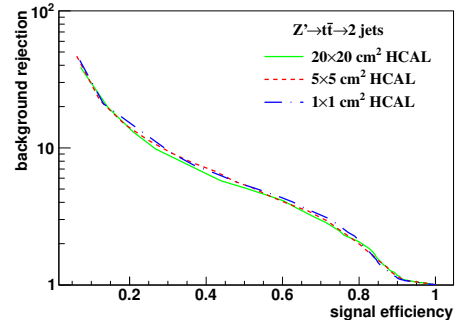


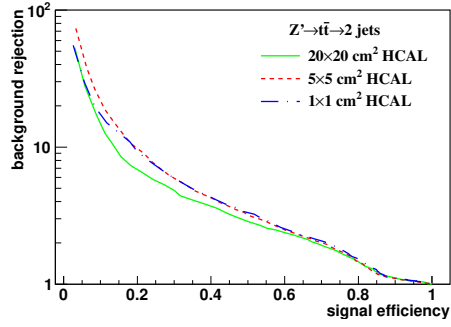
Figure 9: Distributions of soft drop mass for  $\beta=2$ , with 20 TeV c.m. energies and three different detector cell sizes:  $20 \times 20$ ,  $5 \times 5$ , and  $1 \times 1$  ( $\text{cm}^2$ ). The signal (background) process is  $Z' \rightarrow t\bar{t}$  ( $Z' \rightarrow q\bar{q}$ ).



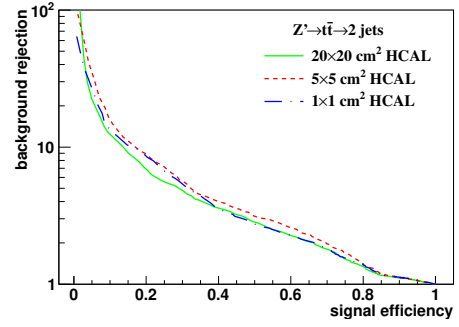
(a)  $Z' (5 \text{ TeV})$



(b)  $Z' (10 \text{ TeV})$



(c)  $Z' (20 \text{ TeV})$



(d)  $Z' (40 \text{ TeV})$

Figure 10: The ROC curves of soft drop mass selection for  $\beta=2$  with 5, 10, 20, 40 TeV c.m. energies. Three different detector cell sizes are compared:  $20 \times 20$ ,  $5 \times 5$ , and  $1 \times 1 \text{ (cm}^2\text{)}$ . The signal (background) process is  $Z' \rightarrow t\bar{t}$  ( $Z' \rightarrow q\bar{q}$ ).

129 with a normalization factor  $d_0$ :

$$d_0 = \sum_k p_{T,k} R_0.$$

130 The  $k$  runs over all constituent particles in a given large radius jet,  $p_{T,k}$  is the transverse  
 131 momentum of each individual constituent particle,  $\Delta R_{j,k} = \sqrt{(\Delta y)^2 + (\Delta \phi)^2}$  is the  
 132 distance between the constituent particle  $k$  and the candidate subjet axis  $j$  in the  $y - \phi$   
 133 plane. The  $R_0$  is the characteristic jet radius used in the anti- $k_t$  jet algorithm.

134 In this analysis, the anti- $k_t$  algorithm with  $R = 0.4$  (AK4) is first employed to re-  
 135 construct jets. The subjet axes are obtained by running the exclusive  $k_t$  algorithm [23]  
 136 and reversing the last  $N$  clustering steps. Namely, when  $\tau_N$  is computed, the  $k_t$  al-  
 137 gorithm is forced to return exactly  $N$  jets. If a large radius jet has  $N$  subjet(s), its  
 138  $\tau_N$  is smaller than  $\tau_{N-1}$ . Therefore, in our analysis, the ratio of the  $\tau_N$  variables,  $\tau_{21}$   
 139 ( $\tau_2/\tau_1$ ) and  $\tau_{32}$  ( $\tau_3/\tau_2$ ), are used to distinguish the one-prong background jets and the  
 140 two-prong jets from W or the three-prong jets from top.

141 We use the ROC curves as described in Section 4.2 to analyze the detector perfor-  
 142 mance and determine the cell size that gives the best separation power to distinguish  
 143 signal from background. Following the suggestion by Ref. [24], requirement on the soft  
 144 drop mass with  $\beta = 0$  is applied before the study of  $N$ -subjettiness. For each detector  
 145 configuration and c.m. energy, the soft drop mass selection is determined as follows.  
 146 First, we look for the median bin of the soft drop mass histogram from simulated signal  
 147 events as described in Section 4.2. Then, we compare the numbers of events in the  
 148 bins adjacent to the medium bin (bin  $i_{\text{med}} - 1$  and bin  $i_{\text{med}} + 1$ ). The bin with larger  
 149 number of events is added, in addition to the medium bin, to extend the mass window.  
 150 The procedure is repeated until the window contains at least 75% of the total number  
 151 of signal events.

152 In order to obtain the signal and background efficiencies, various ranges of the  $\tau_{21}$   
 153 and  $\tau_{32}$  are scanned. Since some of the background distributions have long tails and  
 154 leak into the signal-dominated region, we use the following method as suggested by  
 155 the Pearson Lemma Method [25] to determine the ranges of  $\tau$  variables. First, we take  
 156 the ratio of the signal to background  $\tau_{21}$  ( $\tau_{32}$ ) histograms. The boundaries of the bin  
 157 (seed bin) with maximum signal to background ratio (S/N) give us the first range of  $\tau$   
 158 selection:  $x_{\text{low}}^{\text{seedbin}} < \tau_{21} < x_{\text{high}}^{\text{seedbin}}$ . Then, we compare the S/N in the bins adjacent to  
 159 the seed bin. The bin with larger S/N is added, in addition to the seed bin, to extend  
 160 the  $\tau_{21}$  selection window. Every window has its corresponding  $\epsilon_{\text{sig}}$  and  $1/\epsilon_{\text{bkg}}$  and an  
 161 ROC curve is mapped out.

162 In addition to the ROC curves, we use the so-called "Mann-Whitney" test to quan-  
 163 tify the detector performance. The value of Mann-Whitney is related to the integrated  
 164 area under the ROC curve: if the value is bigger, it indicates the signal and background  
 165 distributions have similar shapes and can not be well separated from each other. Vice  
 166 versa, if the value is smaller, we can achieve a better signal and background separation.

167 Figures 11 and 13 show the distributions of  $\tau_{21}$  and  $\tau_{32}$  for  $\sqrt{s} = 20$  TeV after  
 168 applying requirement on the soft drop mass. The signals considered are  $Z' \rightarrow WW$  ( $\tau_{21}$ )  
 169 and  $Z' \rightarrow t\bar{t}$  ( $\tau_{32}$ ). Figures 12 and 14 present the ROC curves from different detector  
 170 cell sizes and c.m. energies, respectively. The smallest detector cell size ( $1 \times 1$  cm<sup>2</sup>)

171 does not have the best separation power. In fact, in some cases, the best separation  
172 power comes from detector with bigger cell sizes ( $5 \times 5 \text{ cm}^2$  and  $20 \times 20 \text{ cm}^2$ ).

173 Figures 17 (a) and (b) present the summary plots of  $\tau_{21}$  and  $\tau_{32}$  with various detector  
174 cell sizes and c.m. energies using Mann Whitney U test. For  $\tau_{21}$  at smaller c.m.  
175 energies, when cell size is smaller, the detector performance improves. However, when  
176 c.m. energy increases, no improvement is observed using the smallest detector cell size  
177 ( $1 \times 1 \text{ cm}^2$ ). For  $\tau_{32}$ , the case is similar to  $\tau_{21}$ . Even worse, with some c.m. energies,  
178 the bigger detector cell sizes ( $5 \times 5 \text{ cm}^2$  and  $20 \times 20 \text{ cm}^2$ ) have better separation power  
179 than the smallest detector size.

## 180 5.2. Energy correlation function

181 The energy correlation function (ECF) [25] is defined as follows:

$$ECF(N, \beta) = \sum_{i_1 < i_2 < \dots < i_N \in J} \left( \prod_{a=1}^N p_{Tia} \right) \left( \prod_{b=1}^{N-1} \prod_{c=b+1}^N R_{i_b i_c} \right)^\beta, \quad (3)$$

182 where the sum is looped all particles in the jet  $J$ ,  $p_T$  is the transverse momentum of  
183 each individual particle, and  $R$  is the distance between two particles in the  $y$ - $\phi$  plane.  
184 In order to use a dimensionless variable, a parameter  $r_N$  is defined:

$$r_N^{(\beta)} \equiv \frac{ECF(N+1, \beta)}{ECF(N, \beta)}. \quad (4)$$

185 The idea of  $r_N$  comes from N-subjettiness  $\tau_N$ . Both  $r_N$  and  $\tau_N$  are linear in the  
186 energy of the soft radiation for a system of  $N$  partons with soft radiation. In gen-  
187 eral, if the system has  $N$  subjets,  $ECF(N+1, \beta)$  should be significantly smaller than  
188  $ECF(N, \beta)$ . Therefore, we can use this feature to distinguish jets with different num-  
189 ber of subjets. As in Section 5.1, the ratio  $r_N/r_{N-1}$ , denoted by  $C_N$ , (double ratios of  
190 ECFs) is used to study the detector performance:

$$C_N^{(\beta)} \equiv \frac{r_N^{(\beta)}}{r_{N-1}^{(\beta)}} = \frac{ECF(N-1, \beta) ECF(N+1, \beta)}{ECF(N, \beta)^2}. \quad (5)$$

191 In our analysis, we set  $N = 2$  and  $\beta = 1$  ( $C_2^1$ ).

192 Figure 15 presents the histograms of  $C_2^1$  with  $\sqrt{s} = 20 \text{ TeV}$  after making requirement  
193 on the soft drop mass. The signal considered is  $Z' \rightarrow WW$ . Figure 16 shows the ROC  
194 curves from different detector cell sizes for each c.m. energy, respectively. One can see  
195 that the smallest detector cell size ( $1 \times 1 \text{ cm}^2$ ) does not have the best signal/background  
196 separation power. Figure 17(c) summarizes the result of the Mann Whitney U test for  
197  $C_2^1$ . When c.m. energy increases, no improvement is observed from detector with the  
198 smallest cell size.

## 199 Acknowledgements

200 This research was performed using resources provided by the Open Science Grid,  
201 which is supported by the National Science Foundation and the U.S. Department of

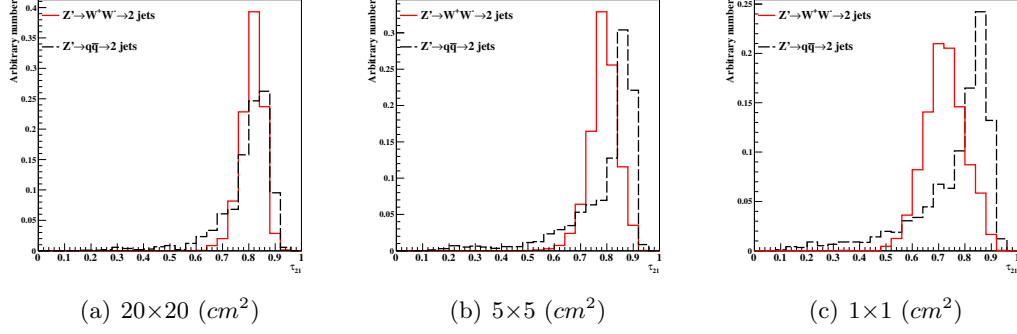


Figure 11: Distributions of  $\tau_{21}$  in 20 TeV energy collision for different detector sizes. Cell sizes in  $20 \times 20$ ,  $5 \times 5$ , and  $1 \times 1 \text{ cm}^2$  are shown here.

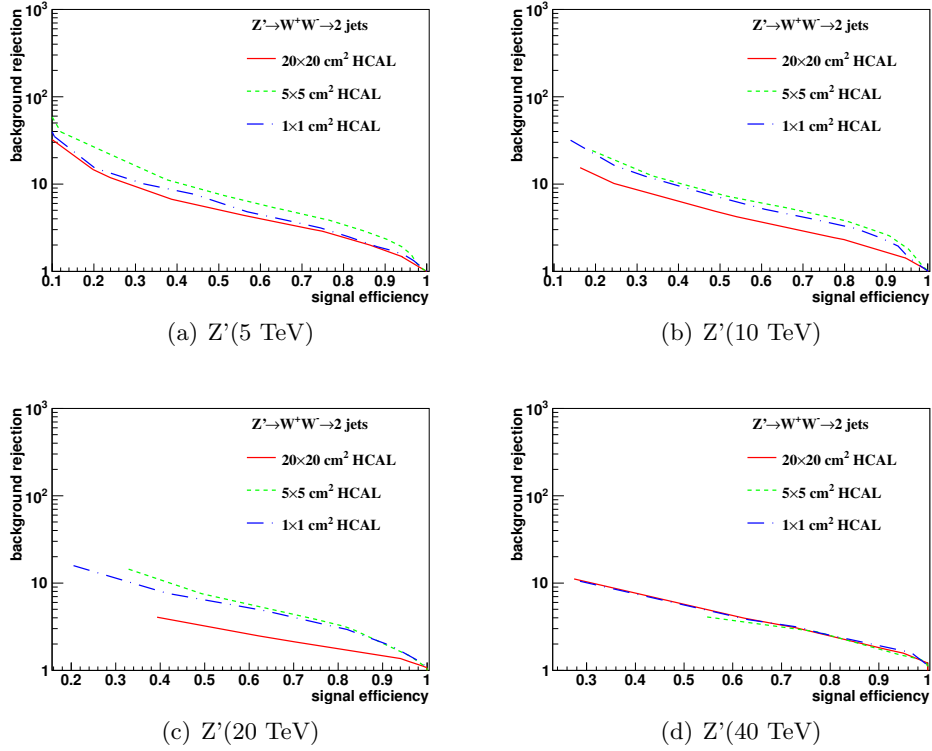


Figure 12: Signal efficiency versus background rejection rate using  $\tau_{21}$ . The energies of collision at (a) 5, (b) 10, (c) 20, and (d) 40 TeV are shown here. In each figure, the three ROC curves correspond to different detector sizes.

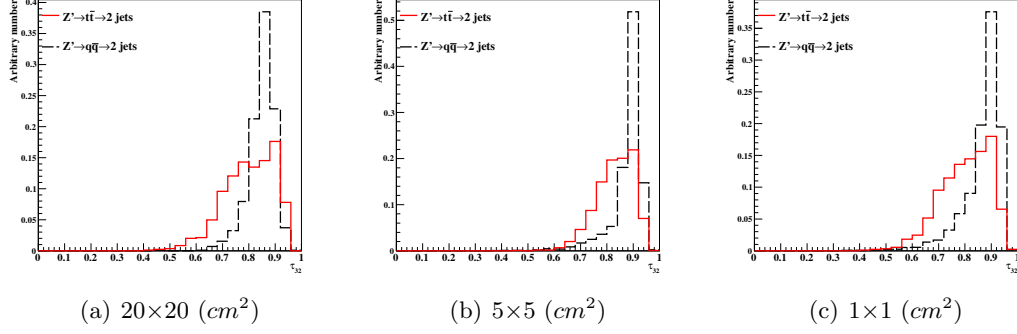


Figure 13: Distributions of  $\tau_{32}$  in 20 TeV energy collision for different detector sizes. Cell sizes in  $20 \times 20$ ,  $5 \times 5$ , and  $1 \times 1 \text{ cm}^2$  are shown here.

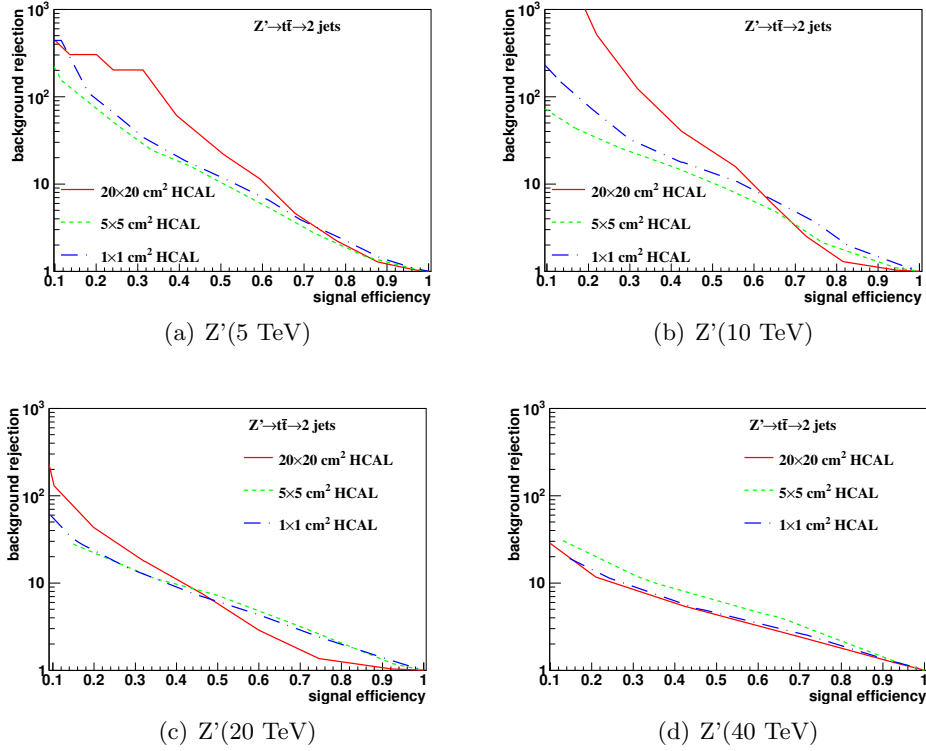


Figure 14: Signal efficiency versus background rejection rate using  $\tau_{32}$ . The energies of collision at (a) 5, (b) 10, (c) 20, and (d) 40 TeV are shown here. In each figure, the three ROC curves correspond to different detector sizes.

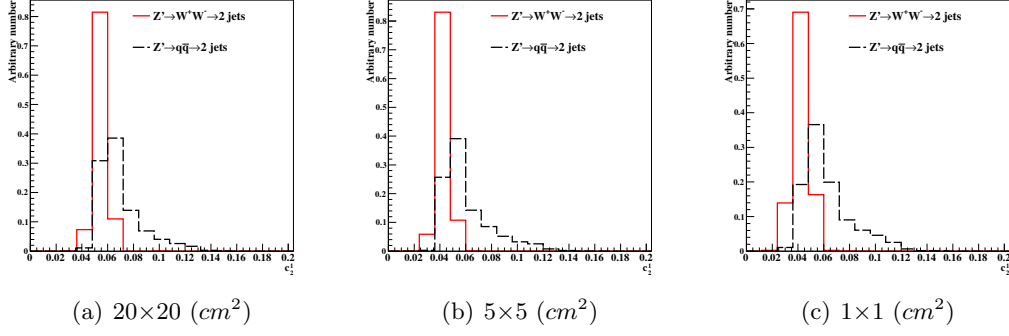


Figure 15: Distributions of  $C_2^1$  in 20 TeV energy collision for different detector sizes. Cell sizes in  $20 \times 20$ ,  $5 \times 5$ , and  $1 \times 1 \text{ cm}^2$  are shown here.

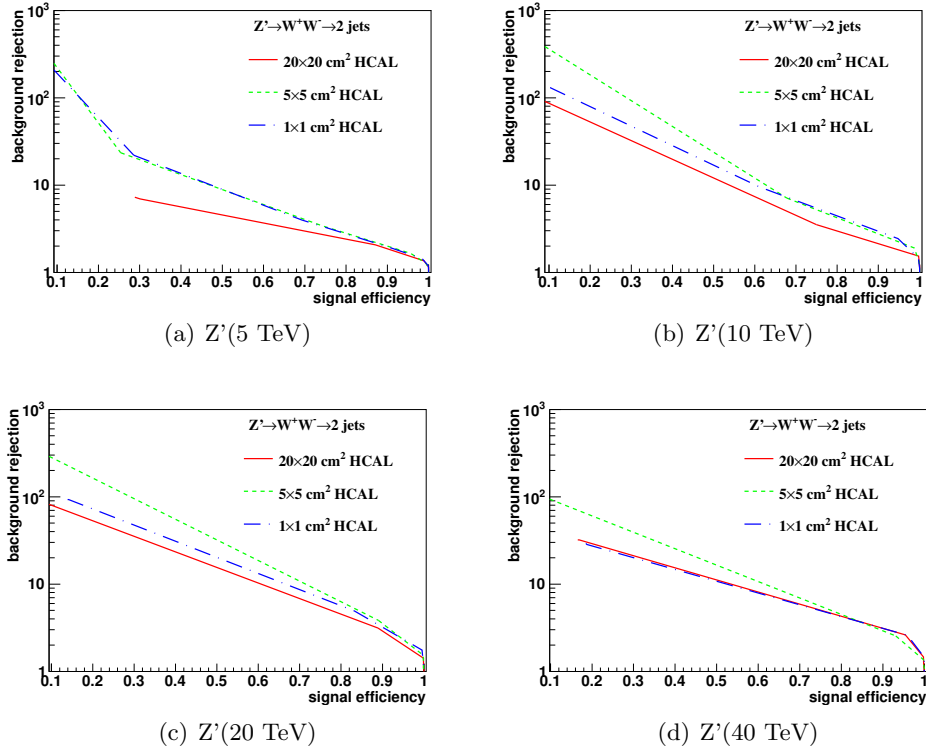


Figure 16: Signal efficiency versus background rejection rate using  $C_2^1$ . The energies of collision at (a) 5, (b) 10, (c) 20, and (d) 40 TeV are shown here. In each figure, the three ROC curves correspond to different detector sizes.

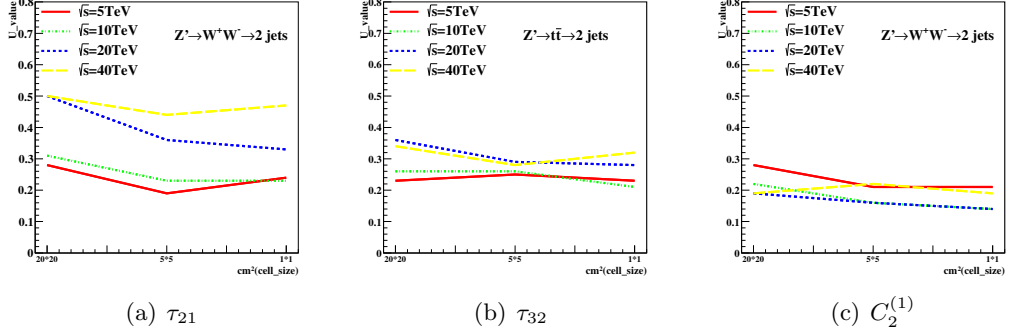


Figure 17: The Mann-Whitney U values for  $\tau_{21}$ ,  $\tau_{32}$ , and  $C_2^{(1)}$  reconstructed with different collision energies and detector cell sizes.

202 Energy's Office of Science. We gratefully acknowledge the computing resources provided  
 203 on Blues, a high-performance computing cluster operated by the Laboratory Computing  
 204 Resource Center at Argonne National Laboratory. Argonne National Laboratory's work  
 205 was supported by the U.S. Department of Energy, Office of Science under contract DE-  
 206 AC02-06CH11357. The Fermi National Accelerator Laboratory (Fermilab) is operated  
 207 by Fermi Research Alliance, LLC under Contract No. DE-AC02-07CH11359 with the  
 208 United States Department of Energy.



## 209 References

- 210 [1] M. Benedikt, [The Global Future Circular Colliders Effort](#) CERN-ACC-SLIDES-2016-0016. Pre-  
211 sented at P5 Workshop on the Future of High Energy Physics, BNL, USA, Dec. 15-18, 2013.  
212 URL <http://cds.cern.ch/record/2206376>
- 213 [2] J. Tang, et al., Concept for a Future Super Proton-Proton Collider (2015). [arXiv:1507.03224](#).
- 214 [3] R. Calkins, et al., [Reconstructing top quarks at the upgraded LHC and at future accelerators](#),  
215 in: Proceedings, Community Summer Study 2013: Snowmass on the Mississippi (CSS2013): Min-  
216 neapolis, MN, USA, July 29-August 6, 2013. [arXiv:1307.6908](#).  
217 URL <https://inspirehep.net/record/1244676/files/arXiv:1307.6908.pdf>
- 218 [4] S. V. Chekanov, J. Dull, Energy range of hadronic calorimeter towers and cells for high-pT jets  
219 at a 100 TeV collider [arXiv:1511.01468](#).
- 220 [5] E. Coleman, M. Freytsis, A. Hinzmann, M. Narain, J. Thaler, N. Tran, C. Vernieri, The importance  
221 of calorimetry for highly-boosted jet substructure [arXiv:1709.08705](#).
- 222 [6] DELPHES 3 Collaboration, J. de Favereau, C. Delaere, P. Demin, A. Giammanco, V. Lematre,  
223 A. Mertens, M. Selvaggi, DELPHES 3, A modular framework for fast simulation of a generic  
224 collider experiment, JHEP 02 (2014) 057. [arXiv:1307.6346](#), [doi:10.1007/JHEP02\(2014\)057](#).
- 225 [7] S. V. Chekanov, M. Beydler, A. V. Kotwal, L. Gray, S. Sen, N. V. Tran, S. S. Yu, J. Zuzelski, Initial  
226 performance studies of a general-purpose detector for multi-TeV physics at a 100 TeV pp collider,  
227 JINST 12 (06) (2017) P06009. [arXiv:1612.07291](#), [doi:10.1088/1748-0221/12/06/P06009](#).
- 228 [8] J. Allison, et al., Recent developments in Geant4, Nuclear Instruments and Methods in Physics  
229 Research A 835 (2016) 186.
- 230 [9] M. J. Charles, PFA Performance for SiD, in: Linear colliders. Proceedings, International Linear  
231 Collider Workshop, LCWS08, and International Linear Collider Meeting, ILC08, Chicago, USA,  
232 November 16-20, 2008 , 2009. [arXiv:0901.4670](#).
- 233 [10] J. S. Marshall, M. A. Thomson, Pandora Particle Flow Algorithm, in: Proceedings, International  
234 Conference on Calorimetry for the High Energy Frontier (CHEF 2013), 2013, pp. 305–315. [arXiv:](#)  
235 [1308.4537](#).
- 236 [11] G. P. S. M. Cacciari, G. Soyez, FastJet user manual CERN-PH-TH/2011-297. [arXiv:1111.6097](#).
- 237 [12] M. Cacciari, G. P. Salam, G. Soyez, The anti-kt jet clustering algorithm, JHEP 0804 (2008) 063.  
238 [arXiv:0802.1189](#).
- 239 [13] S. Chekanov, HepSim: a repository with predictions for high-energy physics experiments, Advances  
240 in High Energy Physics 2015 (2015) 136093, available as <http://atlaswww.hep.anl.gov/hepsim/>.
- 241 [14] B. Auerbach, S. Chekanov, J. Love, J. Proudfoot, A. Kotwal, Sensitivity to new high-mass states  
242 decaying to  $t\bar{t}b\bar{a}$  at a 100 TeV collider [arXiv:1412.5951](#).
- 243 [15] J. Butterworth, B. Cox, J. R. Forshaw,  $WW$  scattering at the CERN LHC, Phys.Rev. D65 (2002)  
244 096014. [arXiv:hep-ph/0201098](#), [doi:10.1103/PhysRevD.65.096014](#).
- 245 [16] S. Catani, Y. L. Dokshitzer, M. H. Seymour, B. R. Webber, [Longitudinally-invariant k-clustering](#)  
246 [algorithms for hadron-hadron collisions](#), Nuclear Physics B 406 (12) (1993) 187 – 224.  
247 URL <http://www.sciencedirect.com/science/article/pii/055032139390166M>
- 248 [17] S. D. Ellis, D. E. Soper, Successive combination jet algorithm for hadron collisions, Phys. Rev.  
249 D48 (1993) 3160–3166. [arXiv:hep-ph/9305266](#), [doi:10.1103/PhysRevD.48.3160](#).
- 250 [18] ATLAS Collaboration Collaboration, G. Aad, et al., Jet mass and substructure of inclusive jets in  
251  $\sqrt{s} = 7$  TeV  $pp$  collisions with the ATLAS experiment, JHEP 1205 (2012) 128. [arXiv:1203.4606](#),  
252 [doi:10.1007/JHEP05\(2012\)128](#).
- 253 [19] J. Thaler, K. Van Tilburg, Identifying Boosted Objects with N-subjettiness, JHEP 03 (2011) 015.  
254 [arXiv:1011.2268](#), [doi:10.1007/JHEP03\(2011\)015](#).
- 255 [20] A. J. Larkoski, S. Marzani, G. Soyez, J. Thaler, Soft Drop, JHEP 05 (2014) 146. [arXiv:1402.2657](#),  
256 [doi:10.1007/JHEP05\(2014\)146](#).
- 257 [21] Y. L. Dokshitzer, G. D. Leder, S. Moretti, B. R. Webber, Better jet clustering algorithms, JHEP  
258 08 (1997) 001. [arXiv:hep-ph/9707323](#), [doi:10.1088/1126-6708/1997/08/001](#).
- 259 [22] M. Wobisch, T. Wengler, Hadronization corrections to jet cross-sections in deep inelastic scattering,  
260 in: Monte Carlo generators for HERA physics. Proceedings, Workshop, Hamburg, Germany, 1998-  
261 1999, 1998, pp. 270–279. [arXiv:hep-ph/9907280](#).
- 262 [23] S. Catani, Y. L. Dokshitzer, M. H. Seymour, B. R. Webber, Longitudinally-invariant  $k_{\perp}$ -clustering  
263 algorithms for hadron-hadron collisions, Nucl. Phys. B 406 (CERN-TH-6775-93. LU-TP-93-2)  
264 (1993) 187–224.

- 265 [24] F. A. Dreyer, L. Necib, G. Soyez, J. Thaler, Recursive Soft Drop, JHEP 06 (2018) 093. [arXiv:](#)  
266 [1804.03657](#), [doi:10.1007/JHEP06\(2018\)093](#).
- 267 [25] A. J. Larkoski, G. P. Salam, J. Thaler, Energy Correlation Functions for Jet Substructure, JHEP  
268 06 (2013) 108. [arXiv:1305.0007](#), [doi:10.1007/JHEP06\(2013\)108](#).